Simulation and visualization of topological defects in nematic liquid crystals

A. C. Callan-Jones* and Robert A. Pelcovits
Department of Physics, Brown University, Providence, Rhode Island 02912, USA

V. A. Slavin, S. Zhang,† and D. H. Laidlaw
Department of Computer Science, Brown University, Providence, Rhode Island 02912, USA

G. B. Loriot
Center for Computation and Visualization, Brown University, Providence, Rhode Island 02912, USA
(Received 30 August 2006; published 12 December 2006)

We present a method of visualizing topological defects arising in numerical simulations of liquid crystals. The method is based on scientific visualization techniques developed to visualize second-rank tensor fields, yielding information not only on the local structure of the field but also on the continuity of these structures. We show how these techniques can be used to first locate topological defects in fluid simulations of nematic liquid crystals where the locations are not known *a priori* and then study the properties of these defects including the core structure. We apply these techniques to simulation data obtained by previous authors who studied a rapid quench and subsequent equilibration of a Gay-Berne nematic. The quench produces a large number of disclination loops which we locate and track with the visualization methods. We show that the cores of the disclination lines have a biaxial region and the loops themselves are of a hybrid wedge-twist variety.

DOI: 10.1103/PhysRevE.74.061701 PACS number(s): 61.30.Jf

I. INTRODUCTION

Topological defects play an important role in condensed matter physics as well as other branches of physics such as particle physics and cosmology. In some systems, particularly two-dimensional systems with continuous order parameter symmetry, topological defects can play an essential role at the phase transition between the ordered (or quasiordered) and disordered phases [1]. Defects also play important roles away from phase transition points—e.g., in the equilibration process following a quench from a disordered to an ordered phase ("coarsening dynamics") [2]. Defects also arise in other physical situations. E.g., in the case of liquid crystals, confinement of the material [3] or the synthesis of inverted nematic emulsions [4] naturally leads to the formation of defects given the interplay between surface anchoring and bulk elastic energy. The dynamics of defects of liquid crystals is also of technological importance—e.g., in displays based on multidomain cells [5,6].

Just as the phase structure of liquid crystals is particularly rich, so is the range and nature of liquid-crystalline topological defects. The stable topological defects of nematics [7] include monopoles and disclination lines. The monopoles are similar to the point defects of the ferromagnetic Heisenberg model, though in the latter case, positive and negative topological charges of the same absolute value are distinct, whereas they are equivalent in the nematic [8]. While defect lines in the ferromagnetic *XY* model can have any integer value with either positive or negative sign, one value of topological charge, 1/2, characterizes the entire class of stable line defects in nematics [7]. All other half-integer-valued lines, whether positive or negative, can be continuously deformed to a line with charge 1/2 and integer-valued lines can "escape in the third dimension" [9]. As in the *XY* model the disclination lines form closed loops or terminate on the surface of the sample because of the prohibitive energy cost of a free line end. While one value of topological charge characterizes the entire class of nematic line defects the director field structure surrounding a defect will depend on the energetics of the system. Figure 1 shows schematic pictures of disclination line segments, illustrating two types of director field patterns, wedge and twist, which can in principle be present. The wedge pattern corresponds to a rotation of the director about an axis parallel to the local direction of the

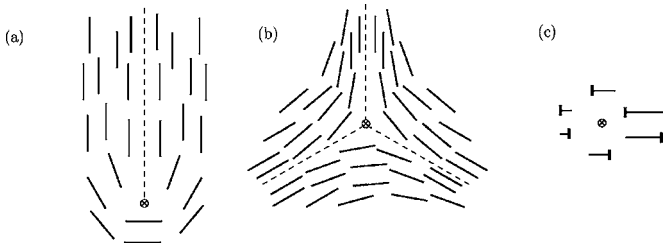

FIG. 1. Schematic drawing of ±1/2 disclination line segments. The disclination cores are indicated by a "⊗," and the disclination line is locally perpendicular to the plane of the page. (a) +1/2 wedge defect, (b) −1/2 wedge defect, and (c) +1/2 twist defect. The rotation of the director in (c) is about an axis lying in the plane of the page perpendicular to the disclination line, and the nail head representation indicates a projection of the director from below the plane of the page. Note that all three defects shown here are topologically equivalent and can be transformed into each other via suitable continuous rotation of the director field.

*Present address: Institut Curie, UMR CNRS 168, 26 rue dUlm 75248 Paris Cedex 05, France.

†Present address: Department of Computer Science and Engineering, Mississippi State University, Mississippi State, MS 39762, USA.

disclination line, while the twist case corresponds to a rotation axis perpendicular to the disclination line direction. Note that intermediate cases where the rotation axis makes an angle with the disclination line not equal to either 0° or 90° are possible. Pure wedge loops carry monopole charge [10–13]. In general, the rotation axis can vary along a disclination line as can the local topological charge.

The far-field structures of nematic defects have been studied within the context of Frank elastic theory [14] and the core structure within the context of the Landau-de Gennes theory [15,16] which uses the complete tensorial nematic order parameter. Numerical simulations of disclination line cores in systems of hard spherocylinders [17–19] have been carried out where the defects were produced by confining the system to a cylinder with homeotropic boundary conditions. In these simulations the position of the defect was known *a priori*. However, it is also of interest to consider situations where the positions of the defects are not known initially or in a situation where the defect moves. E.g., if a liquid crystal system is initialized in the isotropic state and then rapidly quenched below the isotropic-nematic transition temperature, a dense tangle of disclination lines will form and subsequently coarsen over time, a process that has been studied both experimentally [20] and numerically [21]. Locating topological defects in *fluid* simulations where the defect locations have not been predetermined by boundary conditions is a challenging problem. Locating defects in lattice simulations is relatively straightforward. Point defects in two dimensions and line defects in three dimensions can be located by traversing a loop around a primitive square of the lattice. For ferromagnetic spins one measures the rotation of the spin around the square, while for nematics one checks whether the last director traversed is closer to the first director (no half-integer defect) or its antipode (in which case there will be a defect) [22]. Point defects in three-dimensional Heisenberg ferromagnets can be found using the prescription introduced by Berg and Lüscher [23] for the two-dimensional Heisenberg model which was subsequently extended by Lau and Dasgupta [24] to three dimensions.

Several approaches have been taken to track defects in fluid liquid-crystal simulations. In Ref. [21] a thermal quench of a Gay-Berne nematic [25] consisting of 65 536 molecules in a box with periodic boundary conditions was carried out. To track the disclination loops which coarsen and annihilate after the quench, a cubic lattice of bins of molecules was created with the bin size chosen to be approximately equal to the defect core size. This procedure allowed the use of the lattice-defect-finding algorithms described above once an average director for each bin was computed. This method was found to be reliable in locating disclination lines: the lines always formed closed loops and a physically reasonable coarsening sequence emerged after the quench. However, there are many limitations inherent in this approach. First, the defect loops consist of discrete line segments on the dual lattice associated with the bins, so the loops are composed of straight segments joined by 90° corners and the dynamics of the loops is inherently not smooth. Furthermore, all information about the defect core is lost when the bins are created. Another approach [26] that has been used to track defects in simulations of nematic fluids uses Müller matrices to simulate schlieren textures. Like the binning method, the schlieren textures do not show any information about the defect core. Both methods also do not show any information about the nature of the director pattern around the defect: namely, the topological charge of the defect and its wedgelike or twistlike nature.

In this paper we show that scientific visualization methods [27,28] originally developed to study diffusion tensor magnetic resonance imaging of the brain can be modified and then utilized to locate and study disclination lines in simulations of nematic liquid crystals [29,30]. These visualization techniques which were developed to visualize in principle any second-rank tensor field in three-dimensional space yield not only the location of the defect lines but also information about the structure of the defect core and of the director field surrounding the core. These methods can be used with *any* nematic simulation data, irrespective of the underlying model. In this paper we illustrate the utility of these methods by applying them to the Gay-Berne coarsening dynamics data of Ref. [21].

This paper is organized as follows. In the next section we describe the visualization techniques developed to study tensor fields [27,28] and apply them to a nematic liquid crystal. In the following section we show how these techniques when used to analyze the simulation data of Ref. [21] yield the locations and properties of disclination lines. We offer some concluding remarks in the final section.

II. TENSOR FIELD VISUALIZATION

The principal features of the tensor visualization techniques developed in Refs. [27,28] are as follows.

(i) The tensor field must be defined so that its eigenvalues are positive or zero everywhere. The non-negativity of the eigenvalues allows the tensor at a point in space to be viewed as a spheroid whose principal axes and lengths are given by the tensor's eigenvectors and eigenvalues, respectively. The use of spheroids to visualize nematic ordering has been used previously by Andrienko and Allen [18,31]. Uniaxial nematic order corresponds to an ellipsoid whose long axis is parallel to the local nematic director field.

(ii) As obtained from a numerical simulation the tensor field is defined at the location of each molecule. A quasicontinuous tensor field is obtained by introducing a weighting function (see Sec. III below) which yields an interpolated field defined at all points in the simulation volume.

(iii) Three scalar metrics (usually referred to as the Westin metrics [32]) which characterize the tensor field are introduced. As we show below these metrics conveniently provide information on the nature of the nematic order (including biaxiality) and thus can be used to locate disclination lines and characterize their core structure.

(iv) The director field is visualized by the introduction of streamtubes which show the continuity of the local direction of alignment. Stream surfaces are introduced to visualize regions of local planar order. The streamtubes and streamsur-

faces help one visualize the continuity of the spheroids introduced in the first item above.

We now discuss the implementation of these techniques in the case of a nematic liquid crystal. The local nematic order parameter tensor $\mathsf{Q}(\mathbf{r})$ is defined in terms of the unit vector $\hat{\mathbf{u}}^i$ which is parallel to the long axis of molecule i:

$$Q_{\alpha\beta}(\mathbf{r}) = \frac{1}{N(V)} \sum_{i \in V} \left(u_\alpha^i u_\beta^i - \frac{1}{3}\delta_{\alpha\beta} \right), \quad \alpha,\beta = x,y,z, \tag{1}$$

where V is a coarse-graining volume centered on position $\mathbf{r}$ and $N(V)$ is the number of molecules in this volume. The tensor is defined to be traceless so that in a disordered region it will be identically zero. In diagonal form Q is given by

$$\mathsf{Q}^{\mathrm{diag}} = \begin{pmatrix} \frac{2}{3}S & 0 & 0 \\ 0 & -\frac{1}{3}S + \eta & 0 \\ 0 & 0 & -\frac{1}{3}S - \eta \end{pmatrix}, \tag{2}$$

where S is the magnitude of the uniaxial nematic order parameter and η is the biaxiality parameter. With no loss of generality, the rows and columns of $\mathsf{Q}^{\mathrm{diag}}$ can be ordered so that

$$\eta \leqslant S \leqslant -3\eta + 1, \tag{3}$$

$$0 \leqslant \eta \leqslant 1/4. \tag{4}$$

In the isotropic phase, $S = \eta = 0$. In the uniaxial nematic phase, $S \approx 1$, $\eta = 0$. A planar arrangement of otherwise disordered molecules corresponds to $S = \eta$ and an eigenvalue spectrum: $2S/3$, $2S/3$, $-4S/3$. Regions of maximal biaxiality, where the eigenvalues of Q have the largest possible spread consistent with the traceless constraint, correspond to an eigenvalue spectrum: $2S/3$, 0, $-2S/3$.

To implement the visualization techniques we define a modified nematic order parameter tensor D with non-negative eigenvalues by eliminating the last term in Eq. (1):

$$\mathsf{D}^{\mathrm{diag}} = \mathsf{Q}^{\mathrm{diag}} + \frac{1}{3}\mathsf{I} = \begin{pmatrix} \lambda_1 & 0 & 0 \\ 0 & \lambda_2 & 0 \\ 0 & 0 & \lambda_3 \end{pmatrix}, \tag{5}$$

where I is the identity matrix and the eigenvalues of D have been labeled so that

$$\lambda_1 \geqslant \lambda_2 \geqslant \lambda_3. \tag{6}$$

Because the vectors $\hat{\mathbf{u}}^i$ appearing in Eq. (1) are of unit length, we have the condition

$$\mathrm{Tr}\,\mathsf{D} = \lambda_1 + \lambda_2 + \lambda_3 = 1. \tag{7}$$

.

Next, we introduce the three Westin metrics [32]

$$c_l = \lambda_1 - \lambda_2, \tag{8}$$

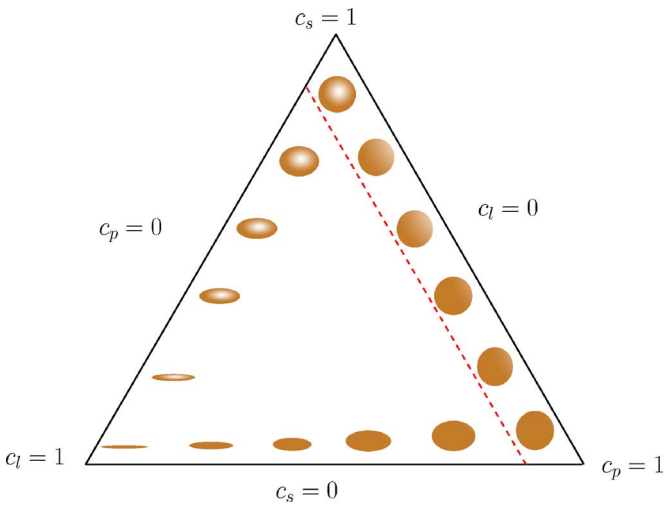

FIG. 2. (Color online) A barycentric coordinate representation of the Westin metrics based on condition, Eq. (12). The dashed line corresponds to $c_l = 0.12$ and separates ordered uniaxial regions outside disclination cores (to the left of the line) from the core regions (to the right of the line). This choice of the numerical value for c_l on the dashed line is explained in the text. The spheroids shown are drawn so that the principal axis directions and lengths are given by the eigenvectors and corresponding eigenvalues of the tensor D [31].

$$c_p = 2(\lambda_2 - \lambda_3), \tag{9}$$

$$c_s = 3\lambda_3, \tag{10}$$

which have the properties

$$0 \leqslant c_l, c_p, c_s \leqslant 1 \tag{11}$$

and

$$c_l + c_p + c_s = 1. \tag{12}$$

.

The condition, Eq. (12), allows a barycentric coordinate representation of the local tensor space, as shown in Fig. 2. Regions of well-ordered unaxial nematic correspond to $\lambda_1 \gg \lambda_2 \approx \lambda_3$—i.e., $c_l \approx 1$; planar ordering corresponds to $\lambda_1 \approx \lambda_2 \gg \lambda_3$—i.e., $c_p \approx 1$; and no order ("isotropy") corresponds to $\lambda_1 \approx \lambda_2 \approx \lambda_3$—i.e., $c_s \approx 1$. Regions to the right of the dashed line in the figure correspond to values of c_l less than a small threshold value. The threshold is chosen by looking at the visualized c_l isosurfaces: starting at $c_l = 0$, where there are no isosurfaces, as c_l is gradually increased isosurfaces begin to emerge which resemble the defect distribution as determined by the method of Ref. [21]. The threshold value is obtained when the isosurfaces are no longer jagged, disconnected pieces, but rather smooth surfaces enclosing the disclination cores. We have chosen $c_l = 0.12$ for this threshold. The spheroids in the figure are drawn so that the principal axis directions and lengths are given by the eigenvectors and corresponding eigenvalues of the tensor D [31], providing a visual signature of the local ordering.

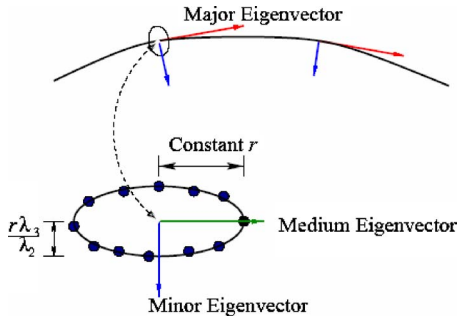

FIG. 3. (Color online) Illustration of a streamtube generated from the trajectory of the major eigenvector corresponding to the largest eigenvalue λ_1. The remaining two eigenvalues λ_2 and λ_3 determine the relative shape of the cross section of the streamtube. The orientation of the cross section is determined by the corresponding eigenvectors. The semiminor axis r along the direction of the medium eigenvector is chosen for visual clarity.

The Westin metrics are related to the uniaxial and biaxial nematic order parameters S and η by

$$c_l = S - \eta, \tag{13}$$

$$c_p = 4\eta, \tag{14}$$

$$c_s = 1 - S - 3\eta, \tag{15}$$

indicating, as one might expect, that uniaxial nematic order with $S \approx 1, \eta \approx 0$ corresponds to $c_l \approx 1$ and a prolate ellipsoid in Fig. 2, while $S \approx 1/4, \eta \approx 1/4$ corresponds to an oblate ellipsoid and $c_p \approx 1$; $S \approx 0, \eta \approx 0$ corresponds to a sphere and $c_s \approx 1$. Regions of maximal biaxality correspond in the case of the D tensor to

$$\lambda_2 = \frac{1}{3}, \tag{16}$$

and $c_s < 1$, to rule out the isotropic case where all three eigenvalues are degenerate.

Stream tubes and streamsurfaces provide a complementary view to the Westin metrics of the nature of the ordering. In particular, they provide a sense of the continuity of the order beyond what would be obtained by drawing spheroids alone. Stream tubes, analogous to stream lines in fluid dynamics, give a representation of the director field in uniaxial regions of the simulation volumes, where c_l is greater than some threshold. The trajectory of a stream tube sweeps along the eigenvector field corresponding to the largest eigenvalue λ_1, and the cross-sectional shape is an ellipse representing the ratio of the other two eigenvalues as shown in Fig. 3. Stream tube seed points are chosen so that streamtubes pass through all regions of c_l greater than the chosen threshold and a selection algorithm culls most of the trajectories and keeps only a representative set [27]. Stream surfaces indicate the local ordering plane in regions where c_p is greater than some threshold. The streamsurface is the approximation of the surface that extends along the eigenvectors corresponding to the two largest and nearly degenerate eigenvalues, λ_1 and λ_2. At any point on a streamsurface, the two eigenvectors lie in the tangent plane to the surface. The integrability of the streamsurfaces can be determined by calculating the Lie bracket of the two eigenvector fields corresponding to the two largest eigenvalues [33]. Additional details about the specific algorithms used to generate the streamtubes and streamsurfaces shown here can be found in Ref. [27].

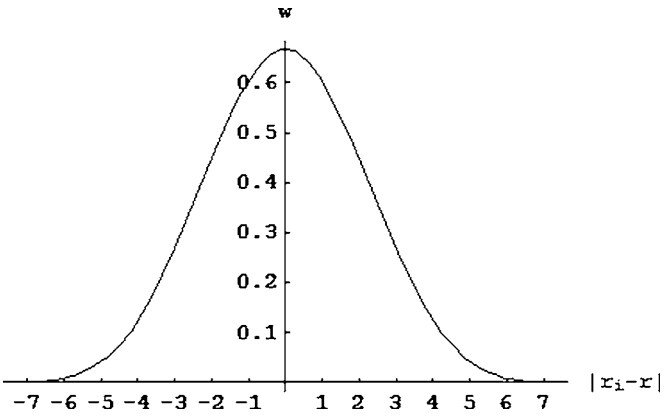

FIG. 4. Illustration of the cubic b-spline weighting function $w(|\mathbf{r}_i - \mathbf{r}|)$ with kernel radius $r_K = 7.3$. The function is constructed in a piecewise continuous fashion such that it is zero outside the kernel radius. Within the kernel $w(x) = \frac{1}{6}(3|x|^3 - 6x^2 + 4), 0 \leq |x| \leq 1; w(x) = \frac{1}{6}(2 - |x|)^3, 1 \leq |x| \leq 2$, where $x = 2|\mathbf{r}_i - \mathbf{r}|/r_K$.

III. RESULTS FOR THE QUENCHED GAY-BERNE NEMATIC

We now show how the visualization techniques outlined in the previous section can be used to obtain physical results from the simulation data of a quenched Gay-Berne nematic [21]. We first smoothed the data by introducing a weighting function $w(|\mathbf{r}_i - \mathbf{r}|)$:

$$D_{\alpha\beta}(\mathbf{r}) = \frac{1}{N(V_S)} \sum_{i \in V_S} w(|\mathbf{r}_i - \mathbf{r}|) u_\alpha^i u_\beta^i, \tag{17}$$

where $N(V_S)$ is the number of molecules in the sampling volume V_S, a sphere of radius r_K centered at point $\mathbf{r}$, and $w(|\mathbf{r}_i - \mathbf{r}|)$ is the sampling weight of a molecule located at $\mathbf{r}_i$, such that

$$\sum_{i \in V_S} w(|\mathbf{r}_i - \mathbf{r}|) = 1. \tag{18}$$

We sampled D at points on a cubic lattice separated by a distance σ_0, the width of a Gay-Berne molecule. We chose the weighting function to be a cubic b-spline [34], a piecewise continuous cubic polynomial approximation to a Gaussian function (Fig. 4), which we scaled so that Eq. (18) is obeyed. The function $w(r_i - r)$ is zero for $|r_r - r| \geq r_K$, where r_K is the kernel radius. We chose $r_K = 7.3$, corresponding to the approximate radius of one coherence volume of the nematic order parameter S [21] (we measure lengths in units of σ_0, the width of the Gay-Berne molecule).

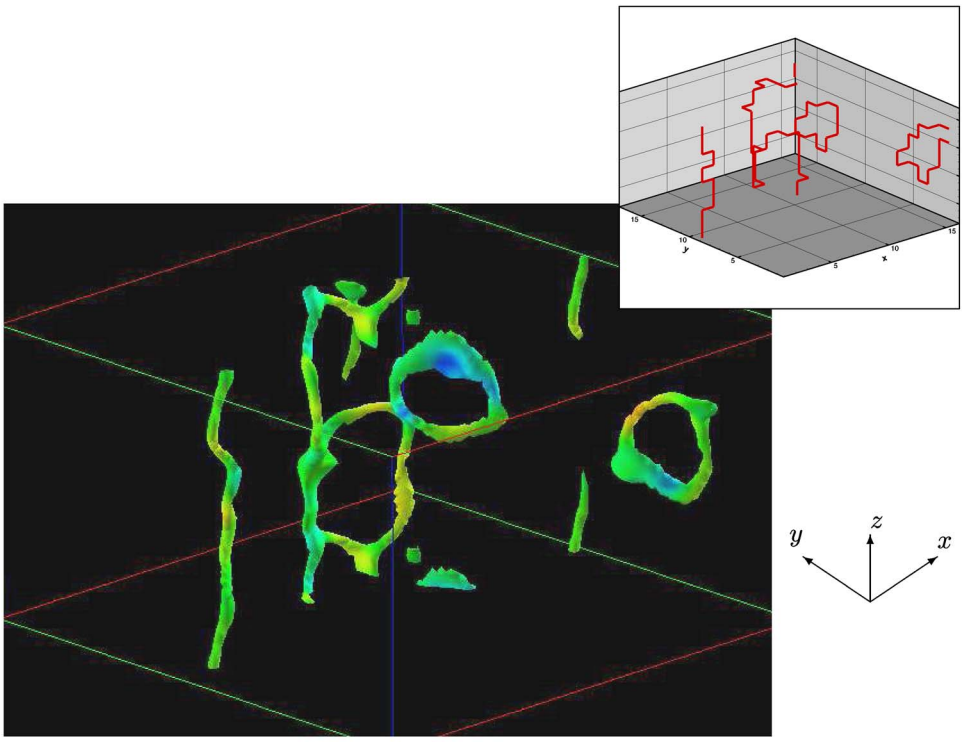

(a)

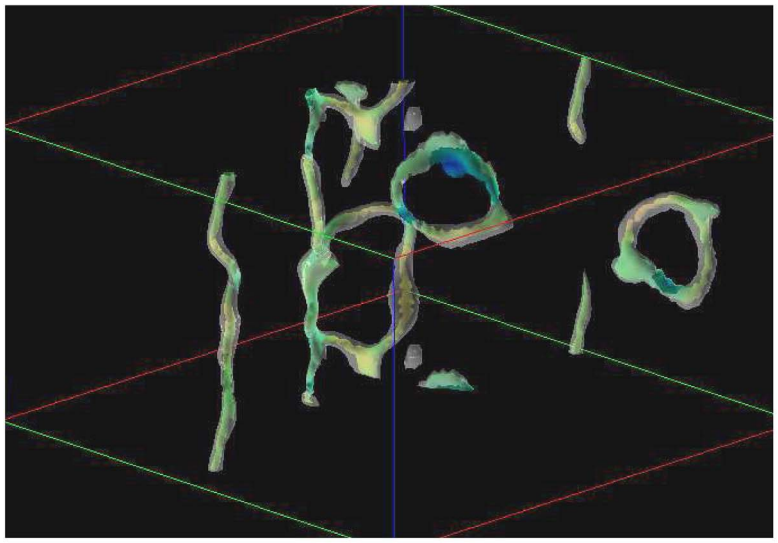

(b)

FIG. 5. (Color online) (a) Visualization of the disclinations in the simulation data of Ref. [21] 35 000 molecular dynamics time steps after an instantaneous thermal quench. The isosurfaces correspond to $c_l=0.12$. The color variation on the c_l isosurfaces indicates variation of c_p, ranging from blue ($c_p \approx 0$) to red ($c_p \approx 0.7$). The inset shows for comparison the disclinations found at the same time step using the method of Ref. [21] which was based on standard lattice techniques. The general locations of the disclinations in the two figures are the same aside from the data padding added to all three directions in the main figure which was done to emphasize the spatial continuity of the disclinations due to periodic boundary conditions. (b) Isosurfaces corresponding to $\lambda_2 = 1/3$, where λ_2 is the intermediate eigenvalue of the tensor D, Eq. (5). This value of λ_2 corresponds to maximal biaxiality of the nematic order parameter tensor.

A. Locations of disclination lines

Figure 5 shows a visualization of the disclination lines in the Gay-Berne nematic [21] 33 000 time steps after a thermal quench from the isotropic to the nematic phase. The disclination lines are identified based on the criterion that the core of a line must be characterized by a very small value of the uniaxial nematic order parameter S or equivalently the Westin metric c_l even if the core is biaxial. The main figure shows isosurfaces of the Westin metric c_l and the intermediate eigenvalue λ_2 using the Advanced Visualization System (AVS) software package [35]. The green-yellow-blue surfaces in the main figure are $c_l=0.12$ isosurfaces; the color variation on these isosurfaces from blue to green to red indicates an increasing value of c_p, a measure of the planar order in the defect core which we discuss further in the next section. Within these isosurfaces $c_l<0.12$ and thus the isosurfaces identify the disclination lines. The inset shows for comparison the same data visualized using the method of Ref. [21] where a cubic lattice of bins was created and disclinations were found using standard lattice techniques [22]. The general locations of the disclination lines in the two figures are the same aside from the data padding added to all three directions in the main figure. The gray isosurfaces surrounding the predominantly green ones correspond to $\lambda_2=1/3$, demonstrating that the disclination cores include a tube of maximal biaxiality, in agreement with the Landau-Ginzburg theory results of Ref. [15].

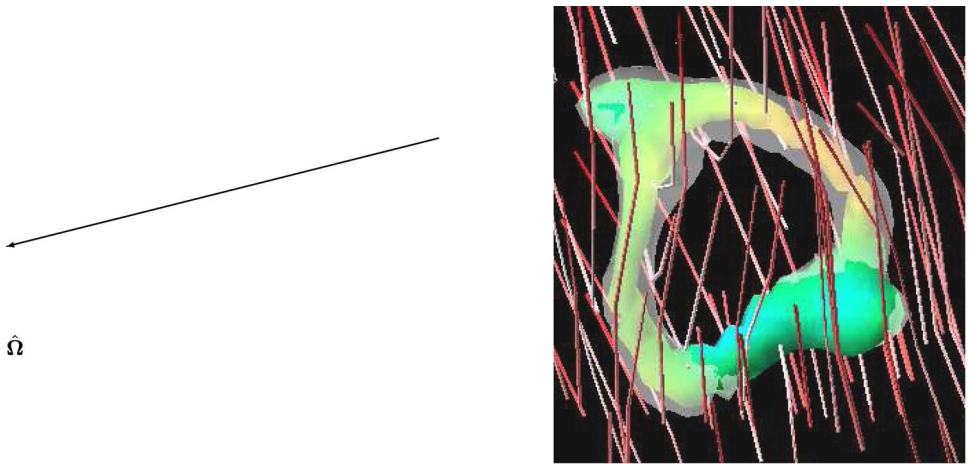

FIG. 6. (Color online) Wedge-twist loop visualized from the data of Ref. [21] 70 000 time steps after the quench into the nematic phase. The green tubelike surface is an isosurface corresponding to $c_l=0.12$ and the red streamtubes (the thin lines) are along the director field. The variation in color along the streamtube indicates the relative value of c_l, with redder corresponding to larger values of this metric (streamtubes were selected so that $c_l \geqslant 0.2$). If one encircles any segment of the loop, the director $\hat{\mathbf{n}}$ rotates about the axis $\hat{\Omega}$.

B. Director structure around dislinations

Stream tubes are particularly helpful in determining the topological charge of a disclination line segment and whether the segment is wedge like or twist like. The latter property is an indication of the direction of the rotation axis of the director (parallel to the disclination line in the wedge case, perpendicular in the twist case, with intermediate possibilites as well) as one encircles the disclination line segment, while the charge is determined by the sense of rotation of the director. Both properties can vary along a disclination loop. Figure 6 demonstrates how streamtubes can help determine the local topological charge and the rotation axis of the director. The time step shown is 148 000 after the thermal quench. The streamtubes wrapping through the loop and around the top of the loop indicate that the top is wedge like with charge $+1/2$ [recall Fig. 1(a)], whereas the streamtubes near the bottom of the loop indicate that this portion is wedge like of charge $-1/2$ [recall Fig. 1(b)]. It is also clear that the disclination loop is twist like on the left side, as the streamtubes have a component parallel to the disclination loop. In fact, this loop is an example of the hybrid type discussed in Ref. [36], where if one encircles any segment of the loop the director $\hat{\mathbf{n}}$ rotates about a spatially uniform axis $\hat{\Omega}$, shown in Fig. 6. Far enough away from the loop $\hat{\mathbf{n}}$ is uniform and perpendicular to $\hat{\Omega}$ and therefore the loop has no monopole charge.

Figure 7 indicates how using streamsurfaces as well as streamsurfaces provides various clues to determine the topological charge and director rotation axis $\hat{\Omega}$ of a disclination that would otherwise be very diffcult to do. From Fig. 7(a) which shows a top view of two relatively straight disclination line segments it might be tempting to conclude that the two disclinations are simply $+1/2$ and $-1/2$ wedge lines. However, examination of the streamtubes and streamsurfaces in a side view of these defects [Fig. 7(b)] shows a more complicated picture. While the disclinations are on average parallel to the z axis, the director field outside the core regions and the planar ordering of the director indicated by the streamsurfaces is considerably tilted out of the x-y plane. A closer view of the $-1/2$ disclination along the line $y=x$ in Fig. 7(c) confirms that this line has twist as well as wedge character. This does not come as a surprise as the twist Frank elastic constant is less than the splay and bend constants in the Gay-Berne nematic [37].

The $+1/2$ and $-1/2$ disclinations shown in Fig. 7(a) remain pinned indefinitely as the simulation progresses as a result of the constraints of the periodic boundary conditions and do not annihilate each other. In the absence of these constraints the annihilation takes place to reduce the elastic energy by achieving a final uniformly ordered state; instead, here the constraints lead to director distortions if the disclinations approach each other too closely. Though this equilibrium is artificially imposed by the periodic boundary conditions, it nevertheless allows us to study properties of disclinations, such as core structure, in greater quantitative detail as we do in the next subsection.

C. Core structure

Figure 8 shows the Westin metrics c_l, c_p, and c_s and the eigenvalue λ_2 scanned along y at fixed x and z for the $-1/2$ and $1/2$ disclinations of Fig. 7(a). The value of x in each case was chosen so that for the fixed value of z (which was chosen to be approximately one-third of the z dimension of the simulation box), the scan along y passes through a global minimum of c_l—i.e., through the center of the defect. Taken together with the appearance of the streamtubes and streamsurfaces in Figs. 7(b) and 7(c), Fig. 8 indicates that the cores of both disclinations become biaxial as the center of the defects is approached from outside [recall that maximum biaxiality corresponds to $\lambda_2=1/3$, Eq. (16)] and at the very center there is strong planar order ($c_p \gtrsim c_s$) in a plane perpendicular to the direction of uniaxial order outside the core. In the language of the original Q tensor, Eq. (2), this planar order

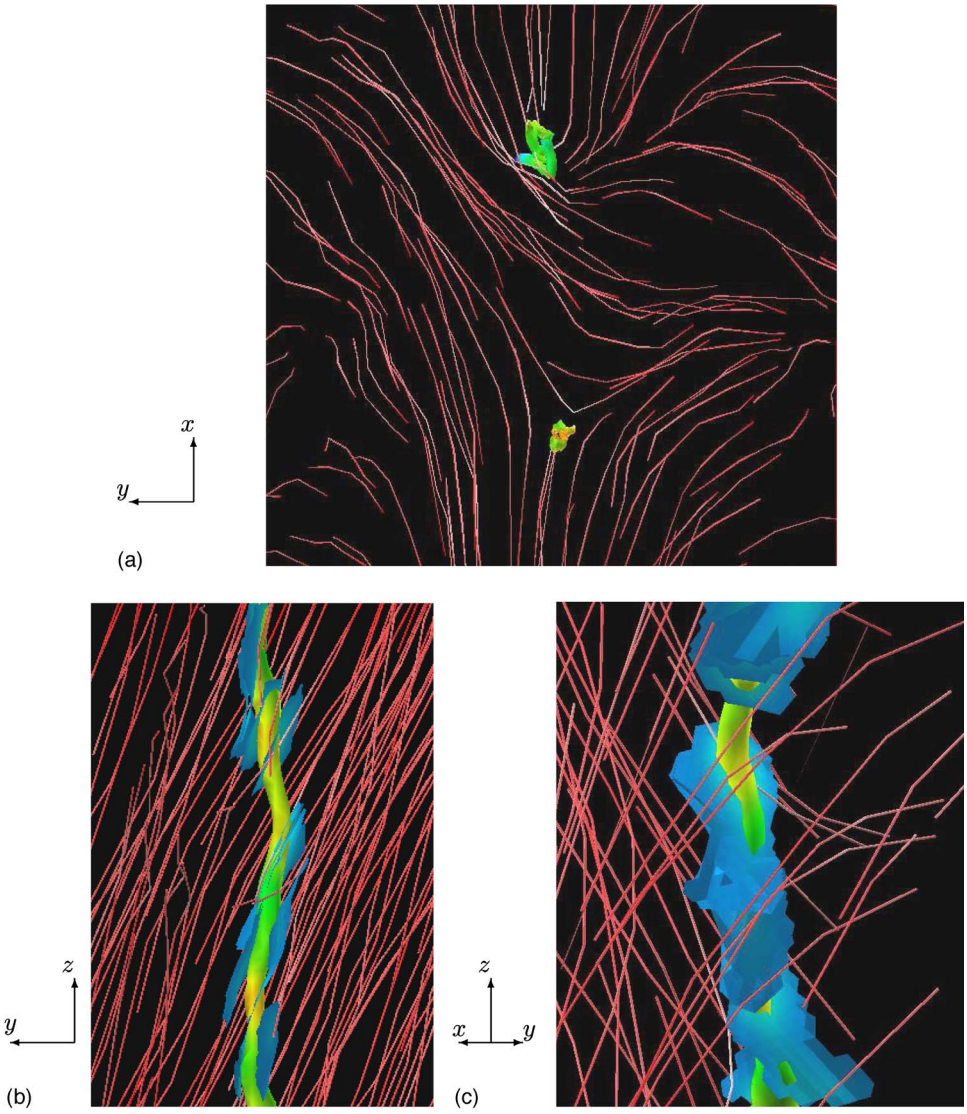

FIG. 7. (Color online) Disclination lines (which form closed loops given periodic boundary conditions) remaining near the end of the simulation of Ref. [21], 70 000 time steps after the quench. In (a) the two lines which are roughly parallel to the z axis are viewed from above and appear to be purely wedge like, with charge $+1/2$ on top and $-1/2$ on the bottom. However, (b) (where the lines are viewed along the x axis) and (c) (where the lines are viewed along the line $x=y$) indicate that the lines have a twistlike character as well. The red streamtubes (the thin lines) show the director field, while the blue streamsurfaces (the flat surfaces) show the planarity of the director field lines near the central portions of the defects indicated by the yellow-green tubelike isosurfaces corresponding to $c_l=0.12$. The color variation on the c_l isosurfaces indicates variation of c_p, ranging from blue ($c_p \approx 0$) to red ($c_p \approx 0.7$). The streamsurfaces, corresponding to $c_p \geqslant 0.2$, intersect the defect lines at regions of relatively high values of c_p. [For conciseness, parts (b) and (c) display only the $-1/2$ line; the $1/2$ line, apart from the sign difference in the topological charge, has a similar twistlike structure.]

corresponds to $S=\eta$ and the largest eigenvalue (in absolute value) of Q equals $-4S/3$. The region of biaxiality surrounding a central core of planar order is precisely what was found in Ref. [15] where the Landau-de Gennes free energy (in a single Frank elastic constant approximation) was minimized as a function of the order parameter tensor Q assuming the presence of a wedgelike disclination line. Figure 8 shows good agreement between our estimate of where maximal biaxiality occurs ($\approx \sigma_0$ away from the defect center) and that of Ref. [15]. Both in our case and Ref. [15], maximal biaxiality occurs at approximately one-tenth the distance between the center of the defect and where the uniaxial nematic order reaches its saturated value outside the core. On the other hand, the degree of planarity in the core of both disclinations shown in Fig. 8 is considerably greater than that predicted analytically in Ref. [15], who found $c_p \approx 0.2$ at the center of their disclination (c_p is given by $2/3$ of the difference between the two smallest eigenvalues of the Q tensor). This difference can probably be attributed to the temperature difference between the simulation of Ref. [21] and the analysis of Ref. [15]. The latter analysis was done at a temperature much closer to T_{NI}, the transition temperature between the nematic and isotropic phases, making planar regions less energetically favorable than comparatively more isotropic ones.

In Fig. 8(a) we see that the ordering in the center of the $-1/2$ defect is more planar than in the center of the $1/2$ defect. It is not completely clear if this is a real equilibrium feature or a fluctuation, as we have found that in exploring other times in the simulation data portions of the core of the $-1/2$ line become more isotropic and portions of the core of the $1/2$ line become more planar. To address this question, Fig. 9 shows c_p at the center of the $+1/2$ and $-1/2$ disclinations, averaged over the entire length of each line, as a function of time. As before we determine the center of the disclination line at height z by finding the minimum value of c_l. We averaged over a time period of 26 500 time steps starting at 70 000 time steps after the quench, keeping data from every 500th time step. By comparison, the coherence time—i.e., the relaxation time for director disturbances to diffuse over a distance σ_0—is approximately 250 time steps

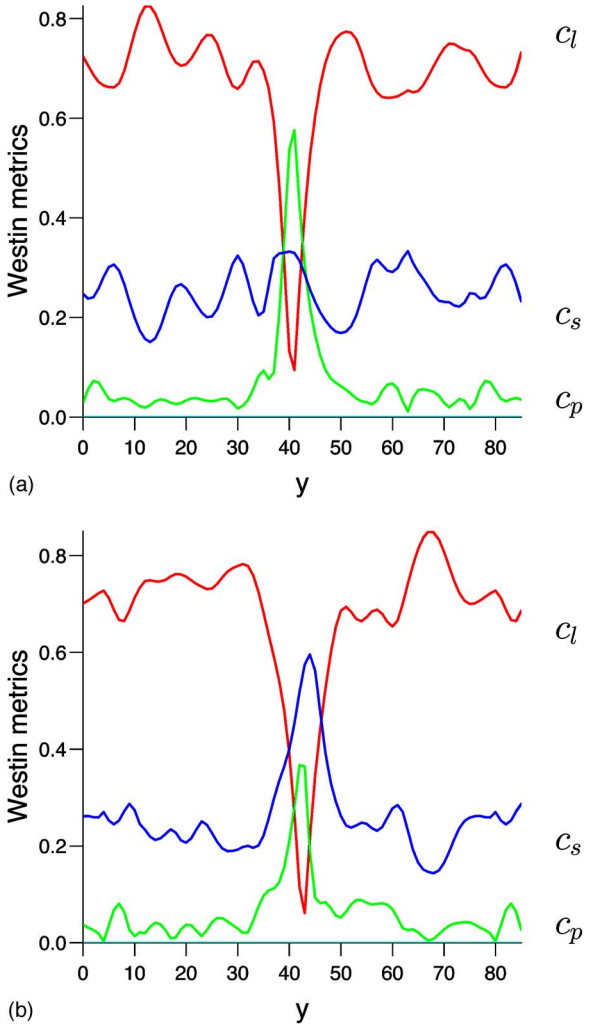

FIG. 8. (Color online) The Westin metrics c_l (red), c_p (green), and c_s (blue) as functions of the coordinate y (in units of σ_0) for the two disclination lines [$-1/2$ in (a), $+1/2$ in (b)] shown in Fig. 7(a). The coordinate system is shown in Figs. 5 and 7(a). The y axis is parallel to one edge of the simulation cell, and the two disclination lines are roughly parallel to the z axis. The value of the x coordinate in the present figure has been chosen to coincide with the center of each line. The fixed value of z is the same in (a) and (b) and is approximately one-third of the z dimension of the simulation box.

in the Gay-Berne system. The initial time corresponds to when the two disclinations have equilibrated with respect to each other; i.e., their separation becomes approximately constant.

The time averages of c_p, indicated by the solid and dashed horizontal lines in Fig. 9, are

$$\langle c_p^+ \rangle = 0.461 \pm 0.007, \tag{19}$$

$$\langle c_p^- \rangle = 0.478 \pm 0.006, \tag{20}$$

where Eqs. (19) and (20) refer to the $1/2$ and $-1/2$ lines, respectively.

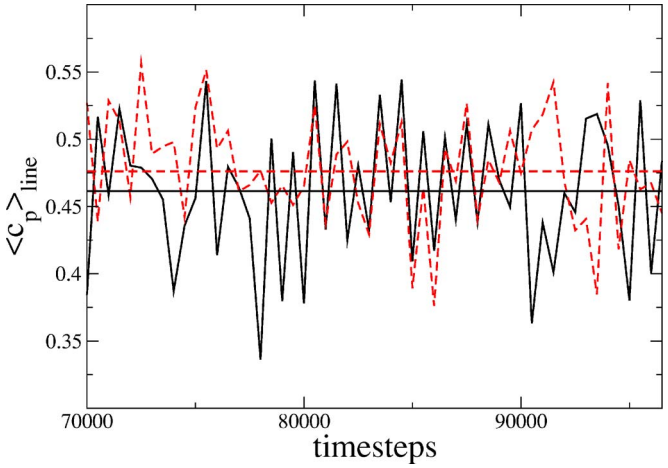

FIG. 9. (Color online) Averages of c_p at center of the disclinations of Figs. 7 and 8 over the entire lengths of the disclination lines, plotted over 26 500 time steps starting at 70 000 time steps after the quench. The value of c_p along the $1/2$ and $-1/2$ disclination lines is indicated by the solid and dashed curves, respectively. The time averages are indicated by the corresponding horizontal lines; the numerical values of these averages are given in Eqs. (19) and (20).

These numbers suggest that the core of the $-1/2$ defect is slightly more planar than the core of the $+1/2$ one. References [15] which uses a single Frank elastic constant approximation for the Landau-Ginzburg energy predicts identical core structure for $+1/2$ and $-1/2$ disclinations, since in this case the elastic free energy is invariant under the rotation of the Q which changes the sign of the charge [38]. It would thus be interesting to extend the analysis of Ref. [15] to study the effect of unequal elastic constants and nonzero far-field twist in the director pattern on the structure of $+1/2$ and $-1/2$ disclination cores.

IV. CONCLUSIONS

In this paper we have presented a method for visualizing topological defects arising in simulations of nematic liquid crystals. The method utilizes scientific visualization techniques originally developed to study the anisotropic diffusion of water in brain tissue. As both anisotropic diffusion and nematic ordering are quantified using second-rank tensor fields, both phenomena can be explored using similar visualization techniques. The visualization method presented here is based on characterizing both the local symmetry of the tensor field (in terms of the Westin metrics) and the continuity of these local properties as one moves through three-dimensional space (in terms of streamtubes and streamsurfaces). These techniques have allowed us to readily elucidate many properties of topological defects that have been up to now difficult, if not impossible, to study using numerical simulation data. The techniques presented here can be used not only to determine the location of defects (as earlier visualization methods could also do) but also to assess the core structure of the defect and director field structure outside the core. It can be readily determined by visual means whether the core is biaxial and whether a disclination line segment is

wedge like or twist like and the sign of its topological charge. Once the visualization methods have identified an interesting region of a simulation cell, it is straightforward to obtain quantitative data as we have illustrated here. While we have illustrated the utility of these visualization techniques using data from a Gay-Berne simulation [21], we emphasize that these techniques can be used with any nematic simulation data, irrespective of the underlying model.

[1] D. R. Nelson, *Defects and Geometry in Condensed Matter Physics* (Cambridge University Press, Cambridge, England, 2002).
[2] A. J. Bray, Adv. Phys. **51**, 481 (2002).
[3] G. E. Volovik and O. D. Lavrentovich, Sov. Phys. JETP **58**, 1159 (1984).
[4] T. C. Lubensky, D. Pettey, N. Currier, and H. Stark, Phys. Rev. E **57**, 610 (1998).
[5] M. Reichenstein, H. Stark, J. Stelzer, and H.-R. Trebin, Phys. Rev. E **65**, 011709 (2002).
[6] J. Chen, P. J. Bos, D. R. Bryant, D. L. Johnson, S. H. Jamal, and J. R. Kelly, Appl. Phys. Lett. **67**, 1990 (1995).
[7] N. D. Mermin, Rev. Mod. Phys. **51**, 591 (1979).
[8] G. E. Volovik and V. P. Mineev, Sov. Phys. JETP **45**, 1186 (1978).
[9] R. B. Meyer, Philos. Mag. **27**, 405 (1973).
[10] A. T. Garel, J. Phys. (Paris) **39**, 225 (1978).
[11] V. P. Mineev, Sov. Sci. Rev., Sect. A **A2**, 173 (1980).
[12] H. Mori and H. Nakanishi, J. Phys. Soc. Jpn. **57**, 1281 (1988).
[13] H. Nakanishi, K. Hayashi, and H. Mori, Commun. Math. Phys. **117**, 203 (1988).
[14] S. Chandrasekhar and G. Ranganath, Adv. Phys. **35**, 507 (1986).
[15] N. Schopohl and T. J. Sluckin, Phys. Rev. Lett. **59**, 2582 (1987).
[16] N. Schopohl and T. J. Sluckin, J. Phys. (Paris) **49**, 1097 (1988).
[17] S. D. Hudson and R. G. Larson, Phys. Rev. Lett. **70**, 2916 (1993).
[18] D. Andrienko and M. P. Allen, Phys. Rev. E **61**, 504 (2000).
[19] J. Dzubiella, M. Schmidt, and H. Lowen, Phys. Rev. E **62**, 5081 (2000).
[20] I. Chuang, R. Durrer, N. Turok, and B. Yurke, Science **251**, 1336 (1991).
[21] J. L. Billeter, A. M. Smondyrev, G. B. Loriot, and R. A. Pelcovits, Phys. Rev. E **60**, 6831 (1999).
[22] M. Zapotocky, P. M. Goldbart, and N. Goldenfeld, Phys. Rev. E **51**, 1216 (1995).
[23] B. Berg and M. Luscher, Nucl. Phys. B **190**, 412 (1981).
[24] M. H. Lau and C. Dasgupta, Phys. Rev. B **39**, 7212 (1989).
[25] J. Gay and B. Berne, J. Chem. Phys. **74**, 3316 (1981).
[26] C. Chiccoli, O. D. Lavrentovich, P. Pasini, and C. Zannoni, Phys. Rev. Lett. **79**, 4401 (1997).
[27] S. Zhang, C. Demiralp, and D. H. Laidlaw, IEEE Trans. Vis. Comput. Graph. **9**, 454 (2003).
[28] A. Vilanova, S. Zhang, G. Kindlmann, and D. H. Laidlaw, in *Visualization and Image Processing of Tensor Fields*, edited by J. Weickert and H. Hagen (Springer-Verlag, Berlin, 2006).
[29] V. A. Slavin, D. H. Laidlaw, R. Pelcovits, S. Zhang, G. Loriot, and A. Callan-Jones, in *VIS '04: Proceedings of the conference on Visualization '04*, edited by H. Rushmeier, G. Turk, and J. J. van Wijk (IEEE Computer Society, Washington, DC, 2004), p. 598.21.
[30] V. A. Slavin, R. Pelcovits, G. Loriot, A. Callan-Jones, and D. H. Laidlaw, in *VIS '06: Proceedings of the Conference on Visualization '06* edited by A. Pang, E. Gröller, and C. Silva (IEEE Computer Society, Washington, DC, USA, 2006).
[31] M. P. Allen, Mol. Simul. **2**, 301 (1989).
[32] C. F. Westin, S. Peled, H. Gudbjartsson, R. Kikinis, and F. A. Jolesz, (unpublished).
[33] S. Zhang, Ph.D. thesis, Brown University, 2006.
[34] R. H. Bartels, J. C. Beatty, and B. A. Barsky, *An Introduction to Splines for use in Computer Graphics and Geometric Modeling* (Morgan Kaufmann, Los Altos, 1987).
[35] C. Upson, J. Thomas Faulhaber, D. Kamins, D. H. Laidlaw, D. Schlegel, J. Vroom, R. Gurwitz, and A. van Dam, IEEE Comput. Graphics Appl. **9**, 30 (1989).
[36] M. Kléman, *Points, Lines, and Walls: In Liquid Crystals, Magnetic Systems, and Various Ordered Media* (Wiley, New York, 1983).
[37] M. P. Allen, M. A. Warren, M. R. Wilson, A. Sauron, and W. Smith, J. Chem. Phys. **105**, 2850 (1996).
[38] P. G. de Gennes and J. Prost, *The Physics of Liquid Crystals*, 2nd ed. (Oxford University Press, Oxford, 1993).